Computational Materials Science 50 (2011) 1365–1371

Contents lists available at ScienceDirect

Computational Materials Science

journal homepage: www.elsevier.com/locate/commatsci

Plastic flow and ductile rupture of a 2198 Al–Cu–Li aluminum alloy

Jianqiang Chen [a], Yazid Madi [a,b], Thilo F. Morgeneyer [a], Jacques Besson [a,*]

[a] Centre des Matériaux, Mines ParisTech, UMR CNRS 7633 BP 87, 91003 Evry Cedex, France
[b] Ermess, EPF-Ecole d'Ingénieurs, Sceaux, France

ARTICLE INFO

Article history:
Received 2 November 2009
Received in revised form 22 June 2010
Accepted 25 June 2010
Available online 24 July 2010

Keywords:
2198 Al–Li
Plastic anisotropy
Ductile rupture
Strain localization

ABSTRACT

Plasticity and fracture mechanisms of a 2198 Al–Cu–Li thin sheet alloy having a thickness equal to 6 mm are investigated. Two heat treatments are studied: T351 and T851. Mechanical tests are carried out on flat specimens including smooth tensile samples and U-notched specimens. Test data are used to identify the parameters of constitutive equations describing plastic anisotropy. The microscopic fracture surfaces of the different specimens are observed using scanning electron microscopy. Smooth and notched samples exhibit a slant fracture surface. Two microscopic fracture mechanisms are identified: fibrous fracture involving grain boundary decohesion and dimple fracture. Observed fracture modes depend on specimen geometry (notches increase stress triaxiality and favor dimple fracture) but also on loading direction. Loading along the rolling direction leads to predominant fibrous fracture. Reducing sheet thickness to 2 mm also favors fibrous fracture. Finally a localization indicator based on Rice's analysis of bifurcation is used to analyse finite element simulations and predict observed fracture plane orientations.

1. Introduction

Increasing payload and fuel efficiency of aircrafts has become a major issue for the aerospace industry and led to the development of materials with high specific mechanical properties. The family of lithium containing Al alloys has received much attention for military, space and commercial application because they offer low density, improved specific strength and high stiffness to weight ratio as compared to the conventional commercial 2xxx and 7xxx series aluminum alloys [1–3]. The marriage of Li to Al offers the promise of substantially reducing the weight of aerospace alloys, since each 1 wt.% Li added to Al reduces density by 3% and increases elastic module by about 6%. Among these series, 2198 Al–Li alloy shows a good combination of static tensile properties, damage tolerance and formability [4,5].

In this study a 6 mm thick sheet of 2198 Al–Li alloy is investigated. Two heat treatments are used: T351 and T851. The paper is organized as follows. First mechanical tests are carried out on smooth and notched flat specimens. A model describing plastic anisotropy is then fitted on these data. Failure mechanisms are investigated using scanning electron microscope (SEM). Finally a strain localization analysis is used to interpret failure patterns.

2. Materials and experiments

2.1. Materials

2198 is a derivate of the alloy 2098, which was developed by McCook Metals to respond to high load on some fuselage parts of the F-16 fighter aircraft [5]. 2198 was developed by Alcan, having slightly lower copper content compared to 2098 and some other minor chemistry adaptations, to optimize toughness. Table 1 gives the chemical compositions limits of 2198 alloy.

For this work, a grade of 2198 Al–Li alloy sheet with a nominal thickness of 6 mm was supplied by Alcan Centre de Recherches de Voreppe (CRV). Rolling induces a specific crystallographic texture and anisotropic mechanical properties so that it is important to keep track of the processing directions. In the following, the rolling direction is referred to as L, the long transverse direction as T and the short transverse direction (thickness) as S. D stands for the diagonal direction (45° between directions L and T in the sheet plane).

The sheet was solution treated, quenched and naturally aged to a substantially stable condition (T3 heat treatment). In this state the material was stretched by 3%. Then an artificial ageing step was preformed to obtain T8 heat treatment. For both heat treatments, specimens having a thickness of 2 mm were prepared by slicing the 6 mm sheet into two halves using electrical discharge machining. Each slice was then machined on both sides to reduce the thickness to 2 mm as proposed in [6,7] to study thickness effect

* Corresponding author.
E-mail address: besson@mat.ensmp.fr (J. Besson).

0927-0256/$ - see front matter © 2010 Elsevier B.V. All rights reserved.
doi:10.1016/j.commatsci.2010.06.029

Table 1
Chemical composition limits of 2198 alloy (wt.%).

Cu	Li	Zn	Mn	Mg	Zr	Si	Ag	Fe
2.9–3.5	0.8–1.1	⩽0.35	⩽0.5	0.25–0.8	0.04–0.18	⩽0.08	0.1–0.5	⩽ 0.01

Table 2
Nomenclature of tested materials.

Material	Heat treatment	Thickness (mm)
$T3F_6$	T351	6
$T3F_{62}$[a]	T351	2
$T8F_6$	T851	6
$T8F_{62}$[a]	T851	2

[a] 6 mm sheet machined down to 2 mm in thickness.

on rupture. Combining heat treatment and thickness results in four different sheets for which a nomenclature is proposed in Table 2.

The optical micrographs of the grain structure after etching with Keller's etch are shown in Fig. 1 for the T3 state. The microstructure consists in flat pancake like grains lying in the L–T plane. The material was also observed using synchrotron radiation computed tomography at ESRF–ID19 (see [8] for details on sample preparation and imaging techniques). This technique allows to evidence white coarse intermetallic phases containing iron and silicon. These phases will act as damage initiation sites during straining of the material. In contrast to other aerospace aluminum alloys [9,10] hardly any initial porosity could be found. T8 ageing is not supposed to affect grain structure or intermetallic coarse phases; thus no general differences compared to the T3 state shown here are expected.

2.2. Mechanical testing

In order to characterize the mechanical behavior, three specimen types were used (Fig. 2). The ST_{12} sample is a conventional smooth flat tensile specimen used to determine the elastic–plastic behavior. Notched samples NT_1 and NT_2 (notch radii equal to 1 and 2 mm respectively) are used to characterize the fracture behavior under various stress triaxiality ratios. The thickness of the specimens corresponds to the sheet thickness (i.e. 2 or 6 mm).

All tests are carried out at room temperature on a 50 kN servo-hydraulic testing machine under displacement control. Tests conducted on smooth specimens are performed along three different

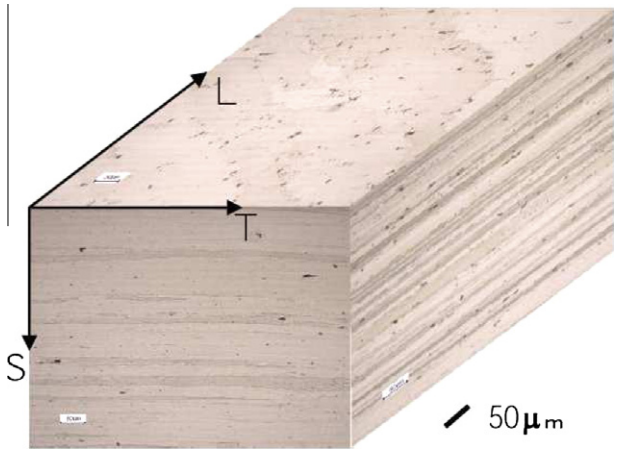

Fig. 1. Microstructure of the material (T3 state): Pseudo-3D image of the grain structure.

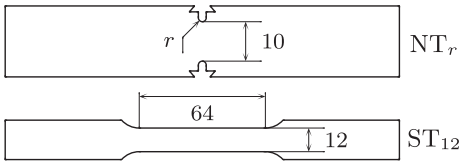

Fig. 2. Specimens for mechanical testing.

directions (L, T and D); U-notched specimens are tested in two directions (L and T). Three specimens at least are tested for each condition. Scatter is negligible so that only one curve is plotted in the following.

Smooth tensile specimens were tested using two displacement gages so that both longitudinal and transverse strain were recorded. For U-notched specimens, opening displacements were measured on both sides and the mean value was used. Tests conducted at different strain rates (10^{-4}–10^{-1} s^{-1}) show that flow stresses tend to slightly decrease with increasing strain rate which indicates the presence of dynamic strain ageing (DSA). In some cases a slight Portevin Le Chatelier (PLC) effect was also observed.

3. Plastic behavior

3.1. Experimental results

Fig. 3a shows the nominal stress (F/S_0) as a function of the plastic elongation for T8F and T3F materials. It is shown that the material presents a strong plastic yielding anisotropy with the L direction being the strongest. The D direction exhibits a much lower yield limit which is typical of Al–Cu–Li alloys [11–13]. The T8 material presents indeed higher yield and ultimate strengths but a lower hardening capability. The T3 material tested along the L direction fails while the load is still increasing and consequently exhibits no necking. This result was reproduced on several test specimens and is not an artifact. Reducing the sheet thickness does not modify the plastic behavior showing that the material does not

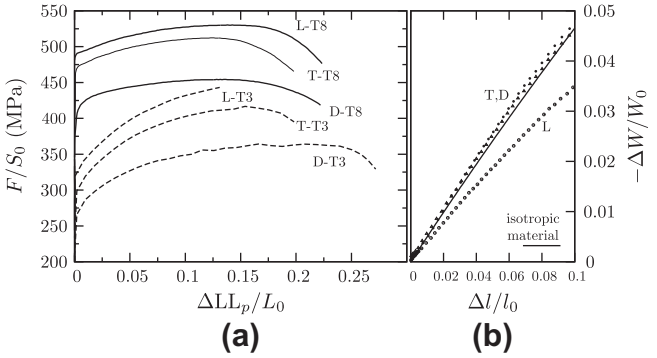

Fig. 3. Tensile tests on ST_{12} specimens along T, L and D directions for the T8F and T3F materials. (a) Nominal stress (F/S_0) as a function of the normalized plastic load line displacement ($\Delta LL_p/L_0$). (b) Width reduction ($\Delta W/W_0$) as a function of the axial strain ($\Delta l/l_0$). (F: force, S_0: initial cross section, ΔLL_p: load line displacement corrected for elastic deformation, L_0: specimen gage length, ΔW: width variation, W_0: initial width, Δl: displacement measured by the longitudinal extensometer, l_0: extensometer gage length.)

Table 3
Tensile properties along the L, T and D directions (YS: yield strength for 0.2% plastic strain (MPa), UTS: ultimate tensile strength (MPa), UE: uniform elongation (%), $\mathscr{L}_k$: Lankford coefficient for a plastic deformation of 5%).

	T3				T8			
	YS	UTS	UE	$\mathscr{L}_k$	YS	UTS	UE	$\mathscr{L}_k$
L	324	442	13.0	0.52	490	530	14.0	0.64
T	300	416	15.4	1.63	470	512	12.3	1.25
D	266	363	21.1	1.0	404	453	13.0	1.06

present a plastic behavior gradient; however failure occurs for lower elongation due to a more pronounced sensitivity to plastic instability [7].

Fig. 3b shows the reduction of the specimen width as a function of the tensile strain (T8F material). Results (dots) are compared with the isotropic case (line) showing a large deviation for the L direction whereas T and D direction are close to the isotropy. These data allow to compute the Lankford coefficient $\mathscr{L}_k$ defined as the ratio of the true deformation along the width of the specimen to the true deformation along the thickness (S direction). The latter is computed assuming plastic incompressibility. Results clearly indicate that for testing along the L direction thickness reduction is higher than width reduction. Similar results were obtained for the T3 material. The principal mechanical characteristics are gathered in Table 3.

Fig. 4 shows for the NT specimens (6 mm thickness) the normalized force (F/S_0) as a function of the notch opening displacement (NOD). As expected the notch leads to an increase of maximum loads compared to smooth tensile specimens. The effect is slightly more pronounced for the more severe notch (NT_1). Note also that the load difference between tests carried out along the L and T direction is smaller than that for tensile tests (Fig. 3). Ductility is smaller for tests carried out along the L direction; the effect is particularly strong for the T3 state; this trend is consistent with results obtained on ST smooth specimens.

3.2. Model

The material under study presents a complex anisotropic plastic behavior which cannot be represented by a simple quadratic yield surface such as the one proposed in [14] which is unable to satisfactorily describe simultaneously yield anisotropy and Lankford coefficients in all directions. To overcome this difficulty, the yield condition proposed by Bron and Besson [15] is used in this work. This phenomenological yield function was developed to represent plastic anisotropy of aluminum alloy sheets. It is an extension of the functions given in Barlat et al. [16] and Karafillis and Boyce [17]. Plastic anisotropy is represented by 12 parameters in the form of two fourth order symmetric tensors. Four other parameters influence the shape of the yield surface uniformly. The model is based on the definition of an equivalent stress $\overline{\sigma}$ function of the stress tensor $\underline{\sigma}$:

$$\overline{\sigma} = \left(\alpha_1 \overline{\sigma}_1^a + \alpha_2 \overline{\sigma}_2^a\right)^{1/a} \tag{1}$$

with $\alpha_2 = 1 - \alpha_1$. $\overline{\sigma}_1$ and $\overline{\sigma}_2$ are respectively given by:

$$\overline{\sigma}_1 = \left(\frac{1}{2}\left(|S_1^2 - S_1^3|^a + |S_1^3 - S_1^1|^a + |S_1^1 - S_1^2|^a\right)\right)^{1/a} \tag{2}$$

$$\overline{\sigma}_2 = \left(\frac{3^a}{2^a + 2}\left(|S_2^1|^a + |S_2^2|^a + |S_2^3|^a\right)\right)^{1/a} \tag{3}$$

where S_1^1, S_1^2 and S_1^3 (resp. S_2^1, S_2^2 and S_2^3) are the eigenvalues of a modified stress deviator $\underline{s}_1$ (resp. $\underline{s}_2$) defined as: $\underline{s}_1 = \underline{\underline{L}}_1 : \underline{\sigma}$ (resp. $\underline{s}_2 = \underline{\underline{L}}_2 : \underline{\sigma}$) where the fourth order tensors $\underline{\underline{L}}_{1,2}$ have the following form using Voigt notation:

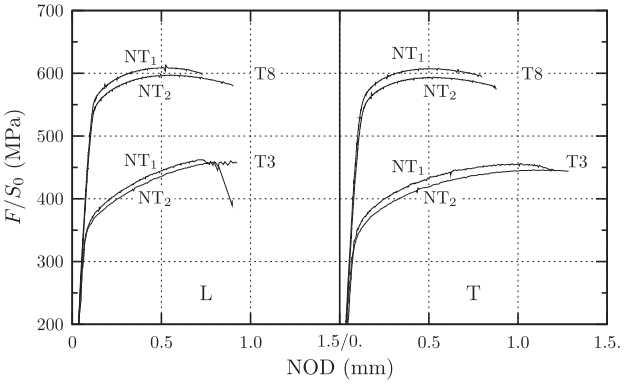

Fig. 4. Normalized force (F/S_0) as a function of the notch opening displacement (NOD) for NT_1 and NT_2 specimens (6 mm thickness).

$$\underline{\underline{L}}_k = \begin{pmatrix} (c_k^{LL} + c_k^{SS})/3 & -c_k^{SS}/3 & -c_k^{LL}/3 & 0 & 0 & 0 \\ -c_k^{SS}/3 & (c_k^{SS} + c_k^{TT})/3 & -c_k^{TT}/3 & 0 & 0 & 0 \\ -c_k^{LL}/3 & -c_k^{TT}/3 & (c_k^{TT} + c_k^{LL})/3 & 0 & 0 & 0 \\ 0 & 0 & 0 & c_k^{TL} & 0 & 0 \\ 0 & 0 & 0 & 0 & c_k^{LS} & 0 \\ 0 & 0 & 0 & 0 & 0 & c_k^{ST} \end{pmatrix} \tag{4}$$

The yield surface is finally expressed as:

$$\Phi = \overline{\sigma} - R(p) \tag{5}$$

where $R(p)$ represents isotropic work hardening parametrized by the effective plastic strain p. R is expressed as: $R(p) = R_0(1 + K_1(1 - \exp(-k_1 p)) + K_2(1 - \exp(-k_2 p)))$.

The identification of the various material parameters was performed following the procedure defined in [15]. In order to identify parameters, tests carried out on ST_{12} specimens (L, T, D loading) and NT specimens (L and T loading) were used (Fig. 3a and Fig. 4). Measured Lankford coefficients (Fig. 3b) were also included in the database. Optimized material parameters are gathered in Table 4 (elasticity and hardening) and Table 5 (anisotropic plastic yield surface) for both materials. A very good agreement between experiments and simulations is obtained as exemplified on Fig. 5 for tensile tests (T8 state) and notched bars tested along the L direction (T3 and T8 states).

4. Failure mechanisms

4.1. Macroscopic failure

Macroscopic fracture surfaces obtained on smooth flat tensile specimens lie in an inclined plane which can be characterized by two angles ϕ and θ as schematically shown on Fig. 6a. Considering a very thin plate under plane stress condition, the theoretical localization angle ϕ_{th} is given by:

Table 4
Parameters describing elasticity and plastic hardening.

	E	ν	R_0	K_1	k_1	K_2	k_2
T3F	74 GPa	0.3	294 MPa	0.022	187	0.775	10.2
T8F	74 GPa	0.3	450 MPa	0.093	655	0.292	16.5

E: Young's modulus, ν: Poisson's ratio

Table 5
Parameters describing anisotropic yielding and plastic flow.

Material	a	α	c_1^{TT} c_2^{TT}	c_1^{LL} c_2^{LL}	c_1^{SS} c_2^{SS}	c_1^{TL} c_2^{TL}	c_1^{LS} c_2^{LS}	c_1^{ST} c_2^{ST}
T3F	17.8	0.716	1.186 0.467	1.028 0.666	0.461 1.478	1.129 1.252	1* 1*	1* 1*
T8F	16.9	0.700	1.152 0.647	1.132 0.756	0.604 1.432	1.183 1.213	1* 1*	1* 1*

* These parameters were *a priori* fixed.

$$\phi_{th} = \frac{\pi}{2} - \arctan\sqrt{\frac{\mathscr{L}_k}{1+\mathscr{L}_k}} \tag{6}$$

Observed fracture angles for T8 condition (2 and 6 mm) are shown on Fig. 6b. For T and D loading ϕ is close to the theoretical value whereas it is equal to 90° for L loading. Note that θ is not equal to 90°. Similar trends are observed for T3-state except in the case of L loading where θ is significantly lower and equal to 36°. Necking is also an important factor to consider. Large necking is obtained for D loading whereas it is less pronounced for L and T loading. Once again L loading for the T3 state is a special case: necking is not observed. Analysing fracture surface on NT specimens is more difficult. However trends in terms of ductility (i.e. necking) and fracture angles are consistent with observations made on ST specimens.

4.2. Fracture mechanisms at the microscopic level

Two main fracture types were observed using SEM (see Fig. 7). The first (type I) one consists in a fibrous fracture surface associated with elongated grains and involving failure at grain boundaries (Fig. 7a). The second one (type II) consists in a classical dimple fracture surface where voids are initiated at iron containing phases. In the case of the investigated materials this type is always associated with the first one as shown on Fig. 7b. Specimens in which a higher stress triaxiality ratio develops are expected to fail by pure dimple fracture.

Pure type I fracture surface is observed for ST specimens tested along L and T direction as well as notched flat specimens in the T3 state and tested along the L direction. In all other cases type II is observed in test specimens. In particular it is present in ST specimens tested along the D direction which exhibit significant necking.

5. Analysis of strain localization

5.1. Rice's localization indicator

In an infinite homogeneous medium, localization is assumed to occur when it becomes possible to form a strain rate discontinuity in a planar band. This band is characterized by its unit normal $\boldsymbol{n}$ and the displacement jump across the band whose direction is denoted $\boldsymbol{g}$. Note that the magnitude of the jump remains unknown.

In the case of elastoplastic materials, the incremental constitutive equation can be expressed as:

$$\dot{\underline{\sigma}} = \underline{\underline{L}} : \dot{\underline{\varepsilon}} \tag{7}$$

where $\underline{\underline{L}}$ is the elastoplastic tangent matrix linking the stress rate $\dot{\underline{\sigma}}$ to the strain rate tensor $\dot{\underline{\varepsilon}}$. Writing the continuity of displacements and the stress equilibrium, it can be shown [18,19] that the jump of the deformation tensor is expressed as: $\frac{1}{2}(\boldsymbol{g}\otimes\boldsymbol{n}+\boldsymbol{n}\otimes\boldsymbol{g})$ and that the condition for bifurcation is written in the case of finite strains (assuming a Jauman stress rate in Eq. (7)) as:

$$\exists \boldsymbol{n},\ \det(\underline{A}(\boldsymbol{n})) = 0 \tag{8}$$
$$\text{with}\quad \underline{A}(\boldsymbol{n}) = \boldsymbol{n}.\underline{\underline{L}}\cdot\boldsymbol{n} + \underline{R}$$
$$\text{and}\quad 2\underline{R} = -\boldsymbol{n}\otimes(\boldsymbol{n}\cdot\underline{\sigma}) + (\boldsymbol{n}\cdot\underline{\sigma})\otimes\boldsymbol{n} + (\boldsymbol{n}\cdot\underline{\sigma}\cdot\boldsymbol{n})\underline{1} - \underline{\sigma}$$

$\boldsymbol{g}$ is then the eigenvector of $\underline{A}(\boldsymbol{n}) + \underline{R}$ corresponding to the eigenvalue equal to zero.

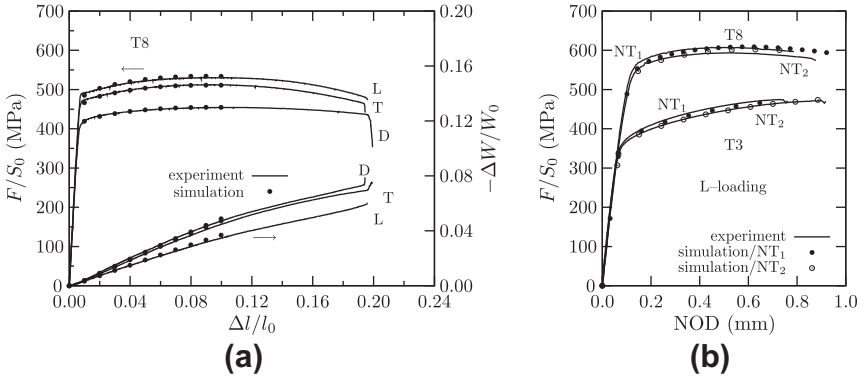

Fig. 5. Comparison of experiments (lines) and simulations (symbols) in the case of tensile tests (a) and NT specimens (b).

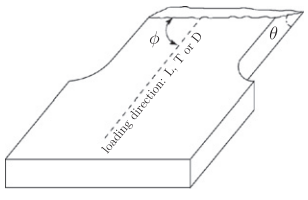

	ϕ	θ	ϕ_{th} (T3)	ϕ_{th} (T8)
L	90°	40–45°	50.9°	52.0°
T	54°	57–65°	58.3°	56.3°
D	57–60°	45–50°	54.7°	55.1°

(b)

Fig. 6. (a) Schematic view of the fracture plane angles ϕ and θ. (b) Observed fracture plane angles (T8) and comparison with the theoretical value for ϕ (Eq. (6)).

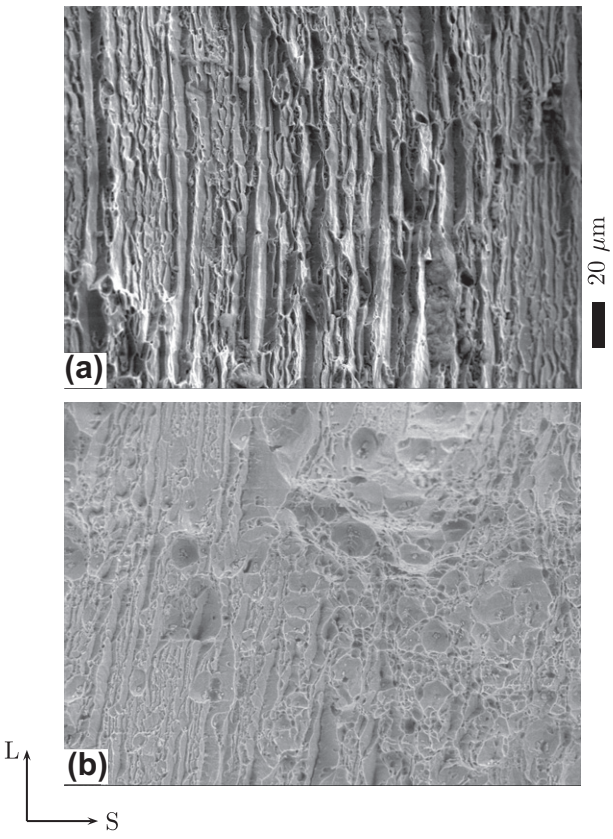

Fig. 7. Microscopic fracture surfaces observed by SEM: (a) Type I: fibrous fracture associated with elongated grains. (b) Type II: mixed dimple/fibrous fracture.

Based on the previous localization condition, a localization indicator can be defined as:

$$I_l = \min_{\boldsymbol{n},\|\boldsymbol{n}\|=1} \det(\underline{A}(\boldsymbol{n})) \tag{9}$$

This indicator can be used to post-process finite element simulations to detect localized zones corresponding to $I_l \leqslant 0$ where fracture is likely to occur [20,21]. The actual localization band orientation does not always correspond to the orientation given by the analysis (i.e. $\boldsymbol{n}$) which assumes a uniform stress and strain state in an infinite medium whereas gradients exist in practical applications.

5.2. Plastic model with damage

Material softening is needed to trigger localization. In this work this is achieved by coupling the anisotropic plasticity model with the Gurson–Tvergaard–Needleman (GTN) model [22–24] as already done in [25,26,10]. The yield surface is now expressed as:

$$\Phi = \frac{\overline{\sigma}^2}{R^2} + 2q_1 f \cosh\left(\frac{q_2}{2}\frac{\sigma_{kk}}{R}\right) - 1 - q_1^2 f^2 = 0 \tag{10}$$

where f represents porosity. q_1 and q_2 are model parameters taken equal to 1.5 and 1, respectively. As tomography does not evidence initial cavities, the initial value for f was taken equal to *0*. On the other hand, voids can be nucleated on intermetallic phases. It is assumed here that strain controlled nucleation linearly generates 1% porosity for plastic strains p up to 0.2; above this limit nucleation stops. Void coalescence is not taken into account in the model. It is assumed that the band first develops and that coalescence and nucleation on a second defect population (e.g. by grain boundary decohesion or by nucleation on strengthening particles) occurs within the band. This is assumed to lead to rapid fracture. This assumption is valid for tensile tests carried out in this study. This would not be the case for cracked specimens where localization bands cannot develop through the entire specimen or for tensile specimens exhibiting cup–cone fracture [20]. As this work only deals with the prediction of fracture patterns, modelling of void coalescence [27] or of nucleation on secondary defects [10] is not necessary.

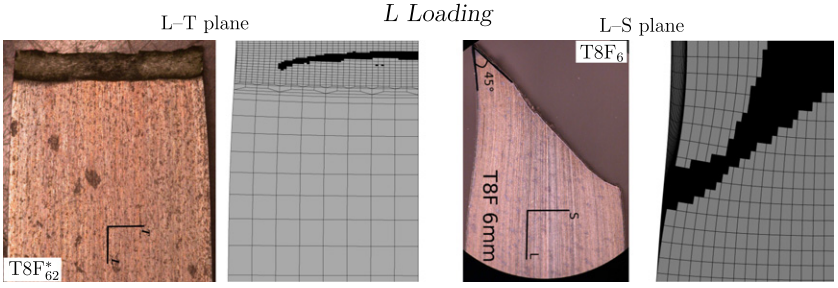

Fig. 8. Experimental and simulated fracture paths for L loading.

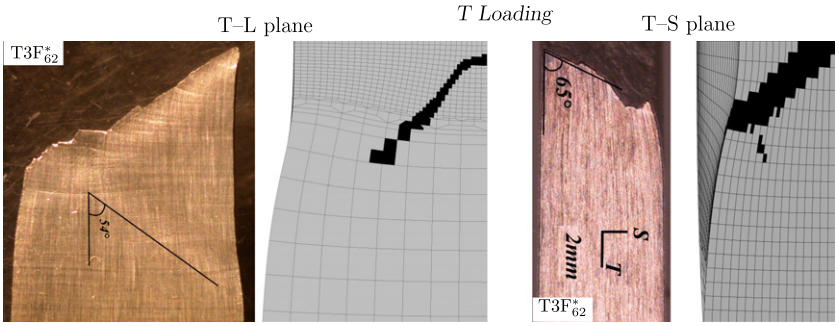

Fig. 9. Experimental and simulated fracture paths for T loading.

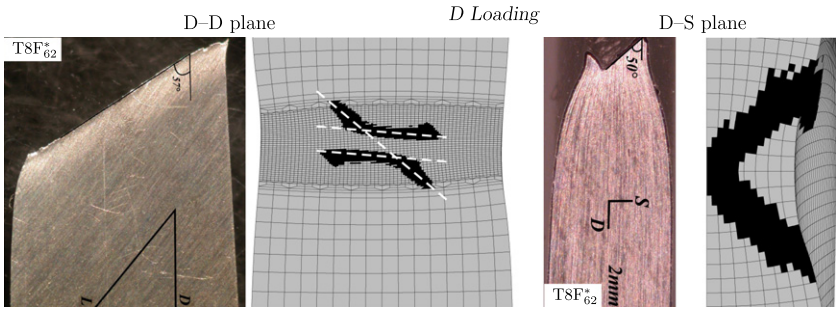

Fig. 10. Experimental and simulated fracture paths for D loading.

5.3. Results

Finite element simulation of the various specimens was performed using the *Zset* software [28,29]. Meshes were constructed using 20 nodes bricks with reduced integration (8 Gauss points). Details about the computation procedure can be found in [20]. Material symmetries were used to reduce the problem size. In the following crack paths are predicted by determining zone where I_l is negative (black areas in Figs. 8–10).

L loading: Fig. 8 compares the experimental and simulated macroscopic fracture paths. A good agreement is found for the T8 condition. In particular the fact that $\phi = 90°$ is well reproduced. This is attributed to the low value of the Lankford coefficient (Table 3) which favors necking along the thickness direction thus leading to almost plane strain state along the T direction. In the case of the T3 condition failure occurs before necking as reported above. Before necking, I_l always remains positive so that failure cannot be predicted by the present analysis. A possible explanation for this anomalous behavior is the presence of DSA and PLC effect. In addition PLC effect [30,31] can be anisotropic thus explaining the difference between L loading and T or D loading.

T loading: Fracture paths are compared on Fig. 9 showing general good agreement. The simulation well reproduces the complex crack orientation.

D loading: This case is more difficult because the problem has fewer symmetries so that half of the specimen must be meshed. The through thickness crack path is well reproduced whereas two different directions are predicted in the sheet plane (white dashed lines on Fig. 10). One of these directions corresponds to the fracture orientation.

Remarks: Considering the thickness reduction at which localization bands can be numerically obtained (Figs. 8–10), the proposed analysis qualitatively reproduces the fact that the local deformation level required to trigger band localization and fracture is low for L loading, intermediate for T loading and high for D loading.

The model is able to predict the localization direction for L loading ($\phi = 90°$, Fig. 8) which strongly differs from that obtained for T loading ($\phi = 54°$, Fig. 9). This result can only be obtained by considering plastic anisotropy. Calculations carried out assuming von Mises plasticity lead to localization direction similar to those obtained for T and D loading.

6. Conclusion

In this study the plastic and fracture behavior of a 2198 Al–Cu–Li alloy sheet subjected to T3 or T8 heat treatment was investigated. Smooth and notched flat tensile specimens were used. Plastic behavior (yielding and flow) is strongly anisotropic; it can be represented by the model proposed in [15]. Macroscopic fracture paths as well as microscopic fracture surfaces were investigated. It is shown that fracture path mainly depends on loading direction and to a lower extend on heat treatment and sheet thickness. A localization indicator based on Rice's bifurcation analysis is used to predict and interpret experimental fracture paths. The analysis shows that failure of smooth flat specimens is essentially governed by anisotropic plasticity which accounts for the differences observed for L (T8) and T or D loading. The analysis also indicates that this failure mechanism does not control failure for L loading in the T3 condition. In that case DSA may be the cause of premature failure before onset of necking.

Acknowledgements

This work is part of a study on third generation Al–Li alloys, research partnership between ALCAN CRV, EADS IW, Mines ParisTech, ENSMA and INPG within the ALICANDTE ANR-project.

References

[1] T.S. Srivatsan, E.J. Lavernia, J. Mater. Sci. Lett. 9 (8) (1990) 888–891.
[2] P. Gomiero, Y. Brechet, F. Louchet, A. Tourabi, B. Wack, Acta Metall. Mater. 40 (1992) 857–861.
[3] C. Giummarra, R.J. Rioja, G.H. Bray, P.E. Magnusen, J.P. Moran, Al–Li alloys: development of corrosion resistant, high toughnessd aluminium–lithium aerospace alloys, in: Proceedings ICAA11 Conference, vol. 1, 2008. pp. 176–188.
[4] A. Heinz, A. Haszler, C. Keidel, S. Moldenhauer, R. Benedictus, W.S. Miller, Mater. Sci. Eng. A 280 (2000) 102–107.
[5] M. Knüwer, J. Schumacher, H. Ribes, F. Eberl, B. Bès, 2198-Advanced aluminium–lithium alloy for A350 skin sheet application, in: Proceedings of 17th AeroMat Conference & Exposition, 2006.
[6] T. Pardoen, Y. Marchal, F. Delannay, J. Mech. Phys. Solids 47 (1999) 2093–2123.
[7] A. Asserin-Lebert, J. Besson, A.-F. Gourgues, Mater. Sci. Eng. A 395 (2005) 186–194.
[8] T.F. Morgeneyer, M.J. Starink, I. Sinclair, Acta Mater. 56 (2008) 1671–1679.
[9] F. Bron, J. Besson, A. Pineau, Mater. Sci. Eng. A 380 (2004) 356–364.
[10] T.M. Morgeneyer, J. Besson, H. Proudhon, M.J. Starink, I. Sinclair, Acta Mater. 57 (13) (2009) 3902–3915.
[11] J. Mizera, J.H. Driveri, E. Jezierka, K.J. Kurzydłowki, Mater. Sci. Eng. A 212 (1996) 94–101.
[12] R. Crooks, Z. Wang, V.I. Levit, R.N. Shenoy, Mater. Sci. Eng. A 257 (1998) 145–152.
[13] D. Steglich, H. Wafai, W. Brocks, Int. J. Damage Mech. 19 (2010) 131–152.
[14] R. Hill, The Mathematical Theory of Plasticity, Clarendon Press, Oxford, 1950.
[15] F. Bron, J. Besson, Int. J. Plasticity 20 (2004) 937–963.
[16] F. Barlat, D.J. Lege, J.C. Brem, Int. J. Plasticity 7 (1991) 693–712.
[17] A.P. Karafillis, M.C. Boyce, J. Mech. Phys. Solids 41 (1993) 1859–1886.
[18] J.R. Rice, The localisation of plastic deformation, in: W. Koiter (Ed.), Proceedings of 14th Internatonal Conference Theoretical and Applied Mechanics, North–Holland, Delft, Amsterdam, 1976, pp. 207–220.
[19] J.R. Rice, The mechanics of earthquake rupture, in: Proceedings of the International School of Physics "Enrico Fermi", North-Holland, 1980, pp. 555–649.
[20] J. Besson, D. Steglich, W. Brocks, Int. J. Solids Struct. 38 (46–47) (2001) 8259–8284.
[21] J. Besson, D. Steglich, W. Brocks, Int. J. Plasticity 19 (10) (2003) 1517–1541.
[22] V. Tvergaard, Adv. Appl. Mech. 27 (1990) 83–151.
[23] J. Besson, Int. J. Damage Mech. 19 (2010) 3–52.
[24] O. Chabanet, D. Steglich, J. Besson, V. Heitmann, D. Hellman, W. Brocks, Comput. Mater. Sci. 26 (2003) 1–12.

[25] F. Bron, J. Besson, Eng. Fract. Mech. 73 (2006) 1531–1552.
[26] B. Tanguy, T.T. Luu, G. Perrin, A. Pineau, J. Besson, Int. J. Pres. Vess. Pip. 85 (5) (2008) 322–335.
[27] A. Benzerga, J. Besson, R. Batisse, A. Pineau, Modell. Simul. Mater. Sci. Eng. 10 (1) (2002) 73–102.
[28] J. Besson, R. Foerch, Comput. Meth. Appl. Mech. Eng. 142 (1997) 165–187.
[29] R. Foerch, J. Besson, G. Cailletaud, P. Pilvin, Comput. Meth. Appl. Mech. Eng. 141 (1997) 355–372.
[30] J. Mizera, K.J. Kurzydlowski, Scr. Mater. 45 (7) (2001) 801–806.
[31] Y.Z. Shen, K.H. Oh, D.N. Lee, Scr. Mater. 51 (4) (2004) 285–289.